



UNIVERSITÀ  
DEGLI STUDI  
DI UDINE

## Università degli studi di Udine

Effects of rotation and buoyancy forces on the flow field behavior inside a triangular rib roughened channel

*Original*

*Availability:*

This version is available <http://hdl.handle.net/11390/1108389> since 2020-02-20T17:03:30Z

*Publisher:*

*Published*

DOI:10.1115/1.4035103

*Terms of use:*

The institutional repository of the University of Udine (<http://air.uniud.it>) is provided by ARIC services. The aim is to enable open access to all the world.

*Publisher copyright*

(Article begins on next page)

# Effects of Rotation and Buoyancy Forces on the Flow Field Behavior Inside a Triangular Rib Roughened Channel

By: Luca Furlani, Alessandro Armellini, Luca Casarsa

Dep. of Electric, Management and Mechanical Engineering – University of Udine –Udine – Italy

Corresponding author: luca.casarsa@uniud.it

## 1 ABSTRACT

2 The flow field inside a triangular cooling channel for the leading edge of a gas turbine blade has  
3 been investigated. The efforts were focused on the investigation of the interaction between effects of  
4 rotation, of buoyancy forces, and those induced by turbulence promoters, i.e. perpendicular square  
5 ribs placed on both leading and trailing sides of the duct. PIV and Stereo-PIV measurements have  
6 been performed for  $Re_{Dh}=10^4$ , rotation number of 0, 0.2, and 0.6, and buoyancy parameter equal to 0,  
7 0.08, and 0.7. Coriolis secondary flows are detected in the duct cross section, but contrary to the  
8 smooth case, they are characterized by a single main vortex and are less affected by an increase of  
9 the rotation parameter. Moreover, their main topology is only marginally sensitive to the buoyancy  
10 forces. Conversely, the features of the recirculation structure downstream the ribs turned out to be  
11 more **sensitive** to both the buoyancy forces and to the stabilizing/de-stabilizing effect on the separated  
12 shear layer induced by rotation.

13 Keywords: blade cooling, internal cooling, rotating channel, buoyancy, rotational effects, PIV

14

## 15 NOMENCLATURE

16	<b>A</b>	<b>channel cross sectional area without ribs</b>
17	<b>Bo</b>	buoyancy parameter
18	<b>Bo<sub>x</sub></b>	<b>buoyancy parameter at a defined x (radial) position</b>
19	<b><math>D_h = 4A/p</math></b>	<b>hydraulic diameter</b>
20	<b>LS</b>	leading side

21	$Nu_0$	Nusselt number computed with Dittus-Boelter correlation
22	$Nu_s$	Nusselt number for the static case of [12]
23	$p$	test section perimeter without ribs
24	$R_x$	radius of rotation
25	$Re_{Dh}$	Reynolds number
26	$Ro$	rotation parameter
27	$T_b$	bulk flow temperature
28	$T_w$	wall temperature
29	TS	trailing side
30	$Tu$	Turbulence intensity computed on $u,v,w$
31	$Tu_{xy'}$	Turbulence intensity computed on $u,v'$
32	$u,v,v',w$	velocity fluctuations on $x, y, y', z$ directions
33	$U_b$	bulk flow velocity
34	$U,V,V',W$	mean velocity components on $x, y, y', z$ directions
35	$x,y,z$	radial, peripheral and normal coordinates
36	$y'$	wall normal direction
37	$\Omega$	rotational speed

38  
39

## 40 1. INTRODUCTION

41 The study about the effects introduced by rotation on the thermal and flow fields inside internal  
42 cooling passages adopted in the rotor blades of gas turbines has recently seen a growing interest in  
43 the research community. Indeed, dedicated test rigs and experimental methodologies have been  
44 developed in the last years with the specific aim to investigate these complex flow and thermal fields.  
45 When a specific cooling passage is subjected to rotation, two are the main physical phenomena that  
46 can have an impact on the coolant path: the rise of Coriolis forces and the appearance of buoyancy

47 effects [1, 2]. The former effect is usually characterized by the rotation parameter defined as  
48  $Ro = \Omega D_h / U_b$  and which takes into account the relative importance between peripheral velocity and  
49 bulk flow velocity. More precisely, the Coriolis acceleration ( $a_c = -2\Omega \times C$ , where  $C$  is the relative  
50 velocity vector) that acts on the relative flow inside the duct causes the establishment of a spanwise  
51 pressure gradient that counterbalances its effects (Fig.1). If a confined flow with non-uniform velocity  
52 distribution is considered, a local unbalance between pressure gradient and Coriolis forces is found  
53 inside the regions of lower momentum fluid, hence a local flow deflection is induced and a secondary  
54 vortical flow establishes in the duct cross section, as sketched in Fig. 1. In the rather common case of  
55 a radial outward flow inside a rectangular channel in orthogonal rotation (i.e. with the rotation axis  
56 parallel to the duct height, **the situation sketched in Fig. 1**), the slower near wall flow is pushed  
57 towards the leading side (LS) of the duct by the Coriolis induced pressure gradient. Consequently, for  
58 continuity, the core fluid is displaced towards the trailing side (TS) of the duct and a symmetrical pair  
59 of vortex cells rises (Fig.1) [3].

60 The second main effect of rotation is described by the buoyancy parameter defined as:

$$61 \quad Bo = Ro^2 \frac{R_x}{D_h} \frac{T_w - T_b}{T_b}$$

62 and which expresses the ratio between buoyancy forces and bulk flow inertial forces. The Bo  
63 parameter is proportional to  $Ro^2$  and depends on the ratio between the local radial position ( $R_x$ ) and  
64 the duct hydraulic diameter ( $D_h$ ). The effect is triggered by a non-uniform fluid temperature, hence  
65 density, distribution that can be characterized by the temperature difference existing between the walls  
66 ( $T_w$ , usually hotter than the fluid) and the bulk flow ( $T_b$ ). More precisely, the hotter (hence with lower  
67 density) near wall fluid experiences a lower centrifugal force than the colder (hence with higher  
68 density) core fluid. This, can alter substantially the flow topology and **consequently** the heat transfer  
69 field with respect to an isothermal situation ( $T_w = T_b$ ).

70 The most recent contributions in literature that deepen the comprehension about these phenomena,  
71 with specific reference to gas turbine cooling channels, deal with the study of the interaction between  
72 rotation effects and those induced by the adoption of turbulence promoters on the channel walls [4].

73 Complex geometries have also been investigated, such as triangular [5], trapezoidal shaped [6, 7] and  
74 multipass channels with bends [8, 9]. For a simplified channel configuration (single-side rib-  
75 roughened rectangular channel with radial outward flow) Coletti et al. [4] showed that the  
76 separating/reattaching flow pattern promoted by the ribs is highly affected by rotation. In particular,  
77 if the background flow vorticity has the same orientation of the angular velocity of the rotating system  
78 (e.g. inside the boundary layer on the LS of a rectangular channel with radial outward flow) a  
79 stabilizing effect on the boundary layer is induced and a wider recirculation area is found downstream  
80 of the obstacles, vice versa occurs at the TS. If non-isothermal conditions are also considered [10],  
81 buoyancy effects cause an higher mixing in the near wall flow, with much higher effects on the  
82 stabilized side wall where the extension of the separated flow region is further increased, conversely  
83 less significant differences are found about the extension of the recirculating flow on the opposite  
84 wall.

85 In the case of rectangular or square channels in orthogonal rotation the basic description about the  
86 rotational effects reported above allows a rather good prediction about the main flow features that  
87 rise inside the passage. On the other hand, if more complex geometries are considered, the analysis  
88 is rather less trivial as shown by [6, 7] for a trapezoidal channel used for trailing edge cooling or in  
89 case of a triangular leading edge passage investigated in [5]. In particular, the latter contribution  
90 showed that inside a smooth triangular channel a non-symmetrical Coriolis vortices pair is found,  
91 with separation and reattachment points that are no longer located about the mid span of the lateral  
92 walls, but are instead located on the triangle upper apexes. Moreover, a steady flow configuration is  
93 never reached, indeed as the flow develops along the channel, more than two Coriolis vortical cells  
94 are found inside the channel cross section. The phenomenon is caused by a periodical reversal of the  
95 spanwise velocity component (i.e. the velocity component normal to both the rotation axis and the  
96 radial direction) inside the low momentum region found at the leading apex. The overall behaviour is  
97 strongly fastened if  $Ro$  is increased.

98 The present work is the first part of a research activity that aims at extending the previous findings

99 about the rotational effects inside triangular shaped ducts by considering also the effects of turbulence  
100 promoters and by introducing buoyancy effects. Indeed, concerning leading edge cooling systems,  
101 the wide open literature provides an abundance of works focused on thermal investigations and rather  
102 complex geometries such as channels with curved walls [11] or systems where cooling is provided  
103 by means of jet impingement combined with coolant extraction [12]. Moreover, if rotating channels  
104 are considered, the availability of results is further reduced in regards of experimental works and flow  
105 field investigations.

106 For the reasons thoroughly explained in the previous discussion on rotation effects in cooling  
107 channels, since information available on simple geometries (i.e. rectangular channel) cannot  
108 straightforwardly apply to more complex ones (i.e. triangular channel), this work frames in the logic  
109 of understanding the main flow features inside triangular channels. The final goal is to create a  
110 background knowledge comparable to the already consolidated on rectangular channels [3, 4, 10] to  
111 deepen the comprehension of the thermal studies.

112 In order to fulfil this purpose, experiments have been conducted on the same rig used by Pascotto et  
113 al. [5] but on a modified test section that allows the heating of the lateral walls that have also been  
114 equipped with square orthogonal ribs. As in Pascotto et al. [5], the choice for this geometry (i.e. a  
115 single passage duct with an equilateral triangle cross section and without extraction holes for film  
116 cooling), beside the previous discussion, is motivated by the availability of a wide thermal analysis  
117 provided in [13, 14] and that can be complemented by the present findings.

118

## 119 **2. TEST RIG AND EXPERIMENTAL METHODOLOGY**

### 120 **2.1 Test rig**

121 The present experimental activity has been conducted on the facility of the Turbomachinery and  
122 Energy Systems Laboratory of the University of Udine. A detailed description of the rig can be found  
123 in [6]. The facility has been designed to allow detailed flow field investigations inside rotating ducts  
124 representative of modern cooling system for gas turbine blades and has been recently upgraded for

125 thermal measurements as well. In particular the system has been provided with a rotary fluidic joint  
126 (Fig. 2(a)) equipped with 32 slip rings used for signal and electric power transmission on board of the  
127 rotating system.

128 The test section consists of a straight channel 820 mm long with an equilateral triangle cross section  
129 of side  $L=130$  mm, (Fig. 2). Square ribs of height  $h=6.5$  mm are placed perpendicularly to the channel  
130 main axis on the two lateral walls. The ribs have a pitch of  $8h$  and have a staggered disposition with  
131 respect to the two channel sides, i.e. with the same geometrical characteristics as in [13, 14]. In order  
132 to investigate buoyancy effects, each ribbed wall has been machined out of a single aluminium slab.  
133 Heating is provided by powering with direct current a  $25\ \mu\text{m}$  thick Inconel sheet attached on the  
134 external surface of the wall (Fig. 2(e)). An external layer of insulating material minimizes the thermal  
135 losses towards the environment. The temperature of each heated wall is monitored with four  
136 thermocouples installed inside the aluminium walls (Figs. 2(c, e)) in the inter-rib regions just  
137 upstream and downstream the investigated area (planes  $yz$  and  $xy'$  in Figs. 2(c, d)). The calibration  
138 of the temperature sensor (connected to the slip rings) and a data averaging process computed on  
139 stencils of 20 samples acquired at 2 Hz lead to an overall uncertainty of  $\pm 0.75$  K. Hot test conditions  
140 have been obtained by heating the ribbed walls up to  $110\ ^\circ\text{C}$ . Differences of 1K have been observed  
141 between the readings of two thermocouples placed on similar points of the same wall but in the two  
142 different inter-rib locations, while the maximum difference between the hottest and the coldest  
143 readings was equal to 5 K and has been observed for tests at the highest rotational speed.

144 The test section is fed with air at ambient conditions through a rotating settling chamber connected  
145 to the rotary fluidic joint. The settling chamber design (Fig. 2(a)) is such that a uniform flow  
146 distribution is ensured at the duct inlet, where a 40mm long honeycomb filter prevents also from flow  
147 separation. At the channel outlet, the exhausted flow is collected in a small settling chamber and then  
148 leaves the test section through a return passage, so avoiding any flow perturbation near the tip region  
149 that could conversely occur under rotation if a free radial outlet was set. The return channel was also  
150 adopted by [13, 14], but in their case it was necessary in order to pressurize the channel and, therefore,

151 to reach very high rotation numbers.

152 All tests were performed with the channel z axis aligned with the **angular velocity**, as depicted in Fig.  
153 2. The test section was spun in both sense of rotation, in order to investigate the flow field on both  
154 leading and trailing sides of the channel without changing the PIV measurement set up (see next  
155 section).

## 156 **2.2 Flow field measurement methodology**

157 Flow field measurements were performed by means of 2D and Stereo-PIV techniques. A single  
158 camera configuration (Fig. 3(a)) for 2D measurements was used on plane  $xy'$  (Fig. 2(d)), while a  
159 double camera configuration (Fig. 3(b)) for Stereo-PIV measurements was used on plane  $yz$  (Fig.  
160 2(c)). The PIV system is custom-made and was already described in [7].

161 The PIV raw data (PIV image pairs) were processed using the commercial software PIVview (from  
162 PIVTEC GmbH). In particular, for the Stereo-PIV data, image back-projection and then stereo  
163 reconstruction were performed; furthermore, a disparity correction was also used in order to minimize  
164 the misalignment errors [15]. Stereo calibration of the measurement chain was achieved inside the  
165 channel by means of multiple images of a target placed at first on the image plane and then displaced  
166 in six adjunctive off-plane positions. The nominal magnification of the PIV images ranges from 17  
167 **pixel/mm** (Stereo-PIV) to 20 **pixel/mm** (2D-PIV), which turns in a vector resolution from 1.06 to 1.25  
168 vectors/mm, respectively.

169 As can be seen from Fig. 3, the present PIV system is fixed, i.e. not rotating with the test section.  
170 Consequently, the measurements at  $Ro > 0$  are carried out in phase-locked mode and, therefore, the  
171 direct output of the PIV raw data is the absolute flow field. The relative field inside the test section is  
172 obtained by subtracting the local peripheral displacement of the system from the PIV data with an ad-  
173 hoc procedure. For the case of PIV measurements conducted on flow planes perpendicular to the  
174 rotation axis, Armellini et. al [16] proposed a specific pre-processing methodology to be applied to  
175 the PIV raw data (image pairs) and that allows to keep the peripheral displacement subtraction error  
176 below 1%, i.e. allows to provide a final accuracy level close to the one of standard 2D measurements

177 on static test sections. Unfortunately, the aforementioned methodology cannot be directly used for the  
178 present case because the selected measurement planes are not perpendicular to the rotation axis (see  
179 position of plane  $xy'$  in Figs. 2(d), 3(a) and 4). Indeed, since a component of the peripheral  
180 displacement lies on the out-of-plane direction (Fig. 4), a correct image reconstruction would need a  
181 precise knowledge of the perspective view realized by the optical system, resulting in a rather  
182 complex implementation of the methodology. In view of this, a different approach has been chosen,  
183 namely the second exposure of each PIV image pair has been pre-processed by applying a rigid  
184 translation of the image in order to reduce the walls' displacement at less than 1 pixel with respect to  
185 the first exposure. This raw peripheral displacement subtraction allows the PIV image processing  
186 algorithm to resolve particle displacements of standard magnitude ( $\pm 10$  pixel) and to impose the  
187 correct boundary conditions on the processing mesh (i.e. no-slip condition at the solid walls).  
188 Successively, the displacement components applied for the rigid image translation are added to the  
189 resulting data in order to restore the absolute velocity field. The post-processing procedure is then  
190 completed by the subtraction of the real peripheral velocity field (the in plane component in Fig. 4),  
191 which is accurately measured as described at the end of this section.

192 The processing of the 2D data is further complicated by the need to compensate for the parallax error  
193 associated to the out-of-plane component of the peripheral displacement (plane  $xy'$  is not  
194 perpendicular to the rotation axis, see Figs. 2(d), 3(a) and 4). More in detail, even if rather long focal  
195 lenses have been used, it is not possible to assume that the light is collected with parallel rays.  
196 Consequently, the out of plane component of the peripheral displacement will be seen by the camera  
197 as an additional in plane displacement (i.e. the parallax error) which magnitude and orientation is  
198 proportional to the distance between a specific measurement point and the intersection of the camera  
199 optical axis with the measurement plane (Fig. 4). Therefore, the peripheral displacement recorded by  
200 the camera, is different from the real in plane one (which can be calculated as  $v = \Omega R \cos(\alpha) \Delta t$ , where  
201  $R$  is the radial position,  $\Omega$  is the measured angular velocity and  $\Delta t$  is the PIV separation time). For the  
202 present data on plane  $xy'$ , the maximum magnitude of the out-of-plane peripheral displacement was

203 14 pixel, hence the resulting in-plane parallax component can be up to 0.9 pixel, which is a not  
204 negligible value. A precise parallax error compensation requires the knowledge of two main input  
205 data: the lenses focal length and the position of the optical axis projection on the image plane. For  
206 sake of accuracy, the actual value of the lens focal length has been directly measured with a dedicated  
207 procedure (i.e. to measure the size of the field of view framed with the present optical configuration)  
208 and turned out to be equal to 108.5 mm.

209 Optical axis projection position has been determined by an in-situ calibration realized with a target  
210 that allows to frame straight lines aligned with the out-of-plane direction on planes either parallel  
211 (Fig. 5(a)) or perpendicular (Fig. 5(b)) to the channel wall. An iterative procedure is carried out by  
212 moving the target until the lines drawn on its surface are seen as points by the camera (procedure  
213 exemplified in figures 5(a, b)), hence defining position of the projection of the camera optical axis on  
214 the image plane. Examples of parallax error compensation displacement fields are reported in Figs.  
215 5(c, d) for the case  $Ro=0.6$ . As can be seen, the projection of the lenses optical axis (highlighted by  
216 the intersection of the two red lines in figures 5(c, d)) has been placed close to the area where flow  
217 recirculation is supposed to be found. This choice guarantees that the most critical area of the analysed  
218 flow field is only marginally affected by the parallax error and by the possible uncertainties of its  
219 compensation. It is worth to mention that the parallax correction has to be applied to the 2D  
220 measurements only, since the Stereo 3D measurements are parallax free by definition.

221 The determination of the peripheral displacement field requires to know the real position of the  
222 measurement points with respect to the rotation axis, the test section angular velocity, and to ensure  
223 a reliable synchronization of the PIV system with the test section angular position. Concerning the  
224 centre of rotation position evaluation, a two steps indirect methodology has been used. As a first step,  
225 the procedure proposed in Armellini et al. [16] is followed, namely a target with a rectangular grid of  
226 dots is placed inside the test section on plane  $z=0$  and it is framed by an auxiliary camera with optical  
227 axis parallel to the axis of rotation (aux camera in Fig. 3(a)). Two exposures of the target are taken  
228 with the test section at two angular positions. The markers centre positions are determined in the two

229 images by means of a cross-correlation with a sample signal and afterwards, the centre of rotation  
230 position can be determined applying a least square method on the markers displacement. Providing  
231 that the number of dots is sufficiently large, the centre of rotation with respect to a reference point of  
232 the target can be located with an accuracy of  $\pm 0.1$  mm. The second step requires to operate the laser  
233 and to acquire an image of the laser sheet trace on the calibrated target. The analysis of this realization  
234 allows to get an accurate determination of the position of the laser sheet trace with respect to the  
235 centre of rotation.

236 The last technical issues that have to be addressed are the synchronization of the PIV system with the  
237 test section rotation and the measurement of the actual peripheral velocity. Both these issues are  
238 solved by sampling the TTL signal from a photodiode (see Fig. 3(b)) periodically screened by the test  
239 section, all the technical details can be found in Armellini et al. [6]. The mean angular velocity for  
240 each revolution,  $\Omega$ , can be computed with a relative error equal to  $\delta\Omega/\Omega=3.5 \times 10^{-7}$ , while image  
241 positioning stability is kept by far smaller than the data spatial resolution (i.e. with image shifts about  
242  $\pm 1$  pixel), so reducing to negligible values the spatial averaging error.

243

### 244 **2.3 Uncertainty analysis**

245 Concerning PIV data accuracy, only statistical flow quantities will be presented, resulting from the  
246 ensemble average of  $10^3$  instantaneous samples. For a static 2D measurement, the overall upper bound  
247 estimate of the mean velocities uncertainty results to be less than 2% with respect to  $U_b$  (95%  
248 confidence level), while the maximum uncertainty in the estimate of the higher order statistics is 5%  
249 of  $U_b$ . For the data acquired under rotation, the pre- and post-processing procedures used for the  
250 peripheral displacement field subtraction introduce further unavoidable error sources that increase the  
251 overall uncertainty on the mean velocities up to 5% of  $U_b$ . A proof of the reliability of this estimation  
252 is provided by Fig. 6, where a cross comparison between 2D and Stereo-PIV data is provided for the  
253 most critical case of  $Ro=0.6$ . The plots clearly show a rather good superimposition of the data with  
254 maximum differences of about  $0.05U_b$ .

## 255 2.4 Test conditions

256 All tests have been conducted at  $Re_{Dh}=10^4$  defined on the duct hydraulic diameter ( $D_h = 75.05$  mm),  
257 on the flow bulk velocity ( $U_b=2.1$  m/s), and flow **properties** measured at the inlet of the test section  
258 (see  $T_{air,in}$  in Fig. 2(c)). Rotation numbers of 0.2 and 0.6 have been reached by spinning the test section  
259 at about 55 and 160 rpm, respectively. **Ribbed walls temperatures of about 110°C corresponded to**  
260  **$Bo=0.08$  and  $0.7$  for the two rotating conditions of  $Ro=0.2$  and  $0.6$ , respectively. The given  $Bo$  values**  
261 **are computed at the radial position where the measurement plane  $yz$  is found ( $R_x=709$  mm, Fig. 2(c)).**  
262 The present working conditions are considered to be representative of current engine conditions and  
263 have been selected in order to be consistent with the available studies [5, 13, 14].  
264 **For computation of  $Bo$ , averaged values of both wall and bulk fluid temperatures have used,** namely  
265 the average of the 8 thermocouples installed inside the aluminium walls for  $T_w$ , and the average  
266 between  $T_{air,in}$  and  $T_{air,out}$  for  $T_b$ . In view of the unavoidable measurement errors and the slightly non-  
267 uniform temperature distribution of the walls previously commented, an uncertainty of  $\pm 5\%$  has to  
268 be considered for the present definition of  $Bo$ . Concerning the computation of  $Re_{Dh}$  and  $Ro$  values,  
269 the main error source comes from the measurement of the air flow rate that causes a final uncertainty  
270 of **about  $\pm 1.5\%$ .**

271

## 272 3. RESULTS

### 273 3.1 2D data on plane $xy'$

274 The characterization of the separation structure downstream of the ribs is obtained by the data  
275 acquired on plane  $xy'$ , i.e. **the plane perpendicular to both the channel wall and the rib axis (Fig. 2(d)).**  
276 Figure 7 reports the reference conditions measured for the static case. The time-averaged stream  
277 tracers' path depicts a separation structure that extends up to about  $x/h=3.5$  and a corner vortex located  
278 on the upstream face of the following obstacle. Contour plots of the in-plane turbulence intensity,

279  $T_{xy} = \frac{1}{U_b} \sqrt{\frac{u^2+v^2}{2}}$ , are reported in Fig. 7(b) **(the white areas that surrounds the ribs and close to the**

280 bottom wall are zones of non valid data, which quality has been spoiled by unavoidable laser light  
281 reflection). As expected, the detected flow features are in agreement with those observed in a  
282 rectangular ribbed channel [17].

283 A summary of the results obtained under rotation is reported in Figs. 8 and 9 in terms of stream tracers  
284 path and  $Tu_{xy}$  levels, respectively (again, blanked regions are not valid data). When the investigated  
285 wall is at the TS (Fig. 8(e-h)), no remarkable effects of both rotation and buoyancy are observed on  
286 the flow topology, with the only exception of a small reduction of the recirculation extension found  
287 for  $Ro=0.6$ . Similar observations are reported also in [10] for the case of a rectangular duct in  
288 orthogonal rotation. The explanation of this behaviour is linked to the destabilizing effect that rotation  
289 has on the separation structure at the TS, which causes rather strong flow turbulence that reduces the  
290 bubble extension and mitigates local density gradients. Also in the present case, higher  $Tu_{xy}$  are  
291 measured at the TS (Fig. 9(e-h)) with respect to both static case (Fig. 7(b)) and LS (Fig. 9(a-d)). More  
292 in detail, the  $Tu_{xy}$  level increases with  $Ro$ , and this effect is enhanced by buoyancy.

293 On the LS, the behaviour is different depending by the  $Ro$  value. At  $Ro=0.2$  (Fig. 8(a, b)), the  
294 separation bubble appears longer than the static case (Fig. 7(a)), in agreement with the stabilizing  
295 effect commented in [10]. Conversely, only marginal buoyancy effects are detected on both flow path  
296 and  $Tu_{xy}$  levels (Fig. 9(a, b)). This is also evident by the profiles of  $\langle uv' \rangle$  extracted at  $y'/h=0.5$  (see  
297 Fig. 2(e)) and reported in Fig. 10(a). Indeed, the comparison of heated/non-heated cases reveals  
298 almost identical behaviours, while the destabilizing/stabilizing effects are rather clear as  
299 demonstrated by the higher values and peaks closer to the obstacle found for TS cases. A different  
300 behaviour is found at  $Ro=0.6$  (Fig. 8(c, d)), where the separation bubble gets only marginally longer  
301 with respect to the static case (Fig. 7(a)) and, unexpectedly, the flow agitation is higher for the non-  
302 heated case than the heated one (Figs. 9(c, d) and 10(b)). Nevertheless, this turned out to be only a  
303 local feature, as it will be clarified later on with the plot of Fig. 14. Finally, it is also worth to observe  
304 that the stream tracers inside the recirculation regions at the LS show a pronounced centripetal path  
305 that is an indication of a relevant 3D character of the flow. This evidence could be at the basis of a

306 possible explanation of the differences commented about the present flow behaviour with respect to  
307 the one found for a rectangular channel [10]. This issue is further discussed in the next section.

### 308 **3.3 3D data on plane yz**

309 Stereo-PIV measurements in plane yz, located at 495 mm from the inlet section (downstream the  
310 honeycomb filter, or 709 mm from the rotation axis, see Fig. 2(c)), have been conducted in order to  
311 characterize the rotational effects on the overall flow structure. In order to ease the present data  
312 analysis, Fig. 11 reports the results found for the smooth, non heated channel configuration obtained  
313 on the same rig and reported in [5]. The Coriolis induced secondary flow is characterized by a vortex  
314 pair at the lowest rotation condition (see vortices A and B in Fig. 11(a)) and shows a remarkable  
315 sensitivity to the change of  $Ro$ . Indeed, at  $Ro=0.4$ , a third vortex (B2 in Fig. 11(b)) appears close to  
316 the LS apex, producing a rather more complex flow distribution. Pascotto et al. [5] provided a  
317 justification of this behaviour and shown how it grows in its complexity as rotation is further  
318 increased. Moreover, the streamwise velocity distribution turned out to be strongly asymmetric, with  
319 higher magnitudes on the TS and a pronounced peak located near the lower apex (Fig 11(c, d)). These  
320 features were associated to the channel thermal behaviour reported in [13].

321 The secondary flow distribution measured inside the ribbed duct is reported in the plots of Fig. 12. A  
322 comparison with the smooth channel case of Fig. 11(a) can be made by looking at the data with the  
323 same sense of rotation (i.e. with the LS on the left, Figs. 12(a)-(d)). With respect to the smooth case,  
324 the clockwise vortex previously found close to the lower apex of the duct (vortex B in Fig. 11(a)) is  
325 now rather bigger and extends almost over all the channel cross section (B in Fig. 12(a)). The counter-  
326 clockwise vortex (A in Fig. 12(a)) is confined close to the upper, non ribbed wall and appears to be  
327 too small to be well captured at the present data resolution. Moreover, the local flow acceleration on  
328 top of the rib (which region is bounded by the 3D separation line that extends all along the rib span  
329 at the TS, see Fig 12(a)) pushes the rotation induced vortices closer to the LS, causing an evident flow  
330 deviation towards the upper wall in the inter rib region at the LS. This is in agreement with the  
331 previous observation about the 3D nature of the separation found behind the obstacle (see comments

332 about Figs. 8(a-d)). Finally, if cases at different  $Ro$  are compared (see Figs. 12(a) and (c)) the  
333 sensitivity of the flow topology on plane  $yz$  to the change of  $Ro$  is practically absent. Moreover, if  
334 heated and non heated cases are compared, no clear effects of the buoyancy are found (see Figs. 12(b,  
335 d) and (a, c)). More evident differences can be instead appreciated in the contour plots of the  $U$   
336 velocity component reported in Figs. 13(a-d) (blanked areas on top of the rib are regions of not  
337 available data due to optical accessibility). Indeed, as  $Ro$  and  $Bo$  are increased, higher velocity peaks  
338 are found at the TS as a consequence of the stronger Coriolis induced secondary structures produced  
339 at higher rotation. The absolute velocity peak on the lower apex that characterize the flow field inside  
340 the smooth channel (Fig. 11(c-d) is instead no longer detected.

341 If the test section is spun in the opposite sense of rotation (Figs. 12(e-h) and 13(e-h)), the Coriolis  
342 induced vortex B is correctly found on the right of the plots and with counter-clockwise rotation, i.e.  
343 close to the LS and pushing core flow toward the TS. Vortex A is again smaller in size and remains  
344 confined close to the upper, non ribbed wall. With respect to the previous comments, the main  
345 differences concern the features of the flow in the inter-rib region at the TS that, conversely to what  
346 happens at the LS, is by far less 3D (Figs. 12(e-h)) and is characterized by a more uniform  $U$  velocity  
347 distribution (Figs. 13(e-h)). Again, slight effects caused by an increase of  $Ro$  and  $Bo$  are found only  
348 in the  $U$  velocity peaks found close to the TS (Figs. 13(e-h)).

349 A final comment about the effect of rotation and buoyancy can be made by looking at the  $Tu$  contour  
350 plots of Fig. 14. The stabilizing/destabilizing effect of rotation can be appreciated by comparing the  
351  $Tu$  levels between leading and trailing sides at the same working conditions (compare frame (a) and  
352 (c) or (b) and (d)), with higher values always observed at the TS. Similarly, the stronger flow mixing  
353 promoted by buoyancy is associated to the overall higher  $Tu$  levels measured for the heated cases  
354 (compare frame (a) and (b) or (c) and (d)). This is not in contrast with the comments about Fig. 10(b).  
355 Indeed also in Fig. 14(b), at the position of plane  $xy'$  (see Fig. 2(d)) the  $Tu$  values for  $Bo=0.7$  are  
356 smaller than those for non-heated case in Fig. 14(a). Therefore, the commented behaviour about the  
357 separated flow length and agitation level at the LS, that differ substantially with respect to the

358 rectangular channel case [10], as to be ascribed to local flow effects that are peculiar of the triangular  
359 geometry, demonstrating once more the need for dedicated analysis.

#### 360 4. THERMAL EFFECTS

361 After providing a description of the time-averaged flow features developing inside the rotating  
362 channel, a further discussion can be addressed concerning the combined effects of rotation and  
363 buoyancy on the thermal performances of the device. This is possible by exploiting the available data  
364 from [14]. Figure 15 reports the thermal data from [14] for a set of flow conditions that are comparable  
365 to those considered in the present work, including also the values at  $Ro=0$ . The plots show the  
366 distributions of the Nusselt number enhancement,  $Nu/Nu_0$  and  $Nu/Nu_s$ , along the channel length and  
367 for variable flow conditions. The  $Nu$  is the result of wall temperature measurements performed in the  
368 experiments while  $Nu_0$  is the one obtained from the Dittus-Boelter correlation and  $Nu_s$  refers to the  
369 static channel case. In Fig. 15, L1/T1 refer to the half portion of the leading/trailing sides close to the  
370 bottom apex, while L2/T2 pertain to the upper half of the leading/trailing sides close to the upper  
371 apexes. The following analysis will be based only on the 3D data on plane yz, since plane xy' is  
372 located just in between of the L1/L2 or T1/T2 zones defined in [14].

373 At first, Figs. 15(a, b) show that rotation sets a substantial increment of Nusselt number in zone T2.  
374 The regions adjacent to the lower apex, L1 and T1, experience also stronger heat transfer although  
375 limited with respect to the upper portion of the TS (i.e. T2). Conversely, zone L2 shows no increment  
376 or even less Nusselt values with respect to the stationary case. The present aerodynamic data can help  
377 to understand this behaviour. The plots in Figs. 12 and 13 show how the L2 region is permanently  
378 swept by the low momentum Coriolis vortex cell, while the adjacent velocity peak favours heat  
379 transfer in region T2. These flow features determine a velocity deficit near the L2 region, hence a  
380 heat transfer deficit with respect the whole channel section and a reduction with respect to the static  
381 case.

382 This flow behaviour, as previously commented in section 3.3, becomes even stronger if the  $Ro$   
383 increases, and consistently does the enhancement factor from [14] (compare data in Fig. 15(a)-higher

384 Ro, with those in Fig. 15(b)-lower Ro).

385 Concerning the Bo effects, [14] shows an overall positive effect, with the highest increment of heat  
386 transfer again located in region T2, Fig. 15(c). Indeed, as demonstrated by the present data, the effect  
387 of buoyancy is an overall augmentation of the turbulent agitation of the flow (Fig. 14), in particular  
388 on the TS. On the contrary, in region L2 this effect is much less pronounced and the turbulent  
389 quantities remains practically unchanged at varying the Bo, consistently with the existence of the low  
390 momentum Coriolis vortex cell above commented.

391

## 392 **CONCLUSIONS**

393 Thanks to the present study, important conclusions are drawn about the buoyancy effects on the flow  
394 field inside a ribbed triangular channel. The main findings are summarized in the following.

395 • Buoyancy forces have only marginal effects that result in increased velocity peaks and in an  
396 overall enhancement of the flow agitation level. No remarkable modifications are found on the  
397 rotation induced secondary flows and on the separation downstream the ribs. This behaviour differs  
398 from the results in [10] for a rectangular channel, where buoyancy lead to a dramatic increase of the  
399 separation length behind the ribs at the LS.

400 • On the duct cross section, rotation induced secondary flows turned out to be strongly asymmetric  
401 and characterized by a single main vortex. Consequently, the present inter-rib flow is characterized  
402 by a condition by far different from the one realized in the region of pairing of two symmetric vortices  
403 that has been investigated by [10] in a rectangular ribbed duct. It is in the authors' opinion that this  
404 evidence is at the basis of the differences here commented.

405 The present analysis once more confirms the complexity of the flow topology inside this kind of  
406 devices, evidence that was already discussed for the smooth case [5]. Therefore, a precise explanation  
407 of the aero-thermal behaviour cannot be based on a simplified conjectured flow model but there is  
408 the need for a deeper understanding. Indeed, the present aerodynamic data allow a precise justification  
409 for the heat transfer performances in rotation that are available in the literature on the same geometry.

410

411 **ACKNOWLEDGEMENTS**

412 This work has been supported by the Italian Ministry of University and Research (MiUR).

413

414 **REFERENCES**

- 415 [1] Johnston J. P., Halleen R. P., Lezius D. K. (1972) *Effects of spanwise rotation on the structure of*  
416 *two-dimensional fully developed turbulent channel flow* J. Fluid Mech. 56, pp. 533–557.
- 417 [2] Morris W. D., Ayhan T. (1979) *Observation on the influence of rotation on heat transfer in the*  
418 *coolant channel of gas turbine rotor blade*, Proc. Inst. Mech. Engrs. 193, pp. 303–311.
- 419 [3] Speziale, C. G., Thangam S. (1983) *Numerical Study of Secondary Flows and Roll-Cell*  
420 *Instabilities in Rotating Channel Flow*, J. Fluid. Mech., 130, pp. 377–395.
- 421 [4] Coletti F., Maurer T., Arts T., Di Sante A., (2012) *Flow field investigation in rotating rib-*  
422 *roughened channel by means of particle image velocimetry*, Exp. Fluids 52, pp. 1043–1061.
- 423 [5] Pascotto M., Armellini A., Mucignat C., Casarsa L. (2014) *Coriolis Effects on the Flow Field*  
424 *Inside a Rotating Triangular Channel for Leading Edge Cooling*, ASME J. Turbomach., 136(3),  
425 p.031019.
- 426 [6] Armellini A., Mucignat C., Casarsa L. (2011) *Flow field analysis inside a gas turbine trailing*  
427 *edge cooling channel under static and rotating conditions*, Int. J. Heat Fluid Flow 32, pp. 1147–1159.
- 428 [7] Mucignat C., Armellini A., Casarsa L., (2013) *Flow field analysis inside a gas turbine trailing*  
429 *edge cooling channel under static and rotating conditions: Effect of ribs*, Int. J. Heat Fluid Flow 42,  
430 pp. 236–250.
- 431 [8] Elfert, M., Schroll, M., Förster, W.(2012) *PIV measurement of secondary flow in a rotating two-*  
432 *pass cooling system with an improved sequencer technique*, Journal of Turbomachinery, 134 (3),  
433 art. no. 031001.

- 434 [9] Lei, J., Li, S.-J., Han, J.-C., Zhang, L., Moon, H.-K. (2014) *Effect of a turning vane on heat*  
435 *transfer in rotating multipass rectangular smooth channel*, Journal of Thermophysics and Heat  
436 Transfer, 28 (3), pp. 417-427.
- 437 [10] Coletti F., Lo Jacono D., Cresci I., Arts T., (2014) *Turbulent flow in rib-roughened channel*  
438 *under the effect of Coriolis and rotational buoyancy forces*, Physics of Fluids 26, p. 045111.
- 439 [11] Domaschke N., von Wolfersdorf J., Semmler K., (2012) *Heat Transfer and Pressure Drop*  
440 *Measurements in a Rib Roughened Leading Edge Cooling Channel*, Journal of Turbomachinery,  
441 134, art. no. 061006
- 442 [12] Andrei L., Carcaschi C., Da Soghe R., Facchini B., Maiuolo F., Tarchi L., Zecchi S., (2013)  
443 *Heat transfer measurements in a leading edge geometry with racetrack holes and film cooling*  
444 *extraction*, Journal of Turbomachinery, 135 (3), art. no. 031020
- 445 [13] Liu Y.H., Huh M., Rhee D.H., Han J.C., Moon H.K.K. (2009) *Heat Transfer in Leading Edge,*  
446 *Triangular Shaped Cooling Channels With Angled Ribs Under High Rotation Numbers*, ASME J.  
447 Turbomach., 131(4), p. 041017.
- 448 [14] Liu Y.H., Huh M., Han J.C., Moon, H.K. (2010) *High Rotation Number Effect on Heat Transfer*  
449 *in a Triangular Channel With 45 deg, Inverted 45 deg, and 90 deg Ribs*, ASME J. Heat Trans., 132(7),  
450 p. 071702.
- 451 [15] Willert, C.(1997), *Stereoscopic Digital Particle Image Velocimetry for Application in Wind*  
452 *Tunnel Flows*,” Meas. Sci. and Technol., 8, pp. 1465–1497
- 453 [16] Armellini, A., Mucignat C., Casarsa L., Giannattasio P., (2012) *Flow field investigations in*  
454 *rotating facilities by means of stationary PIV systems*, Meas. Sci. Technol. 23, p.025302 (11pp).
- 455 [17] Rau, G., Moeller, D., Cakan, M., Arts, T., (1998) *The effect of periodic ribs on the local*  
456 *aerodynamic and heat transfer performance of a straight cooling channel*, ASME J. of  
457 Turbomachinery, 120, pp 368-375.

Figure 1

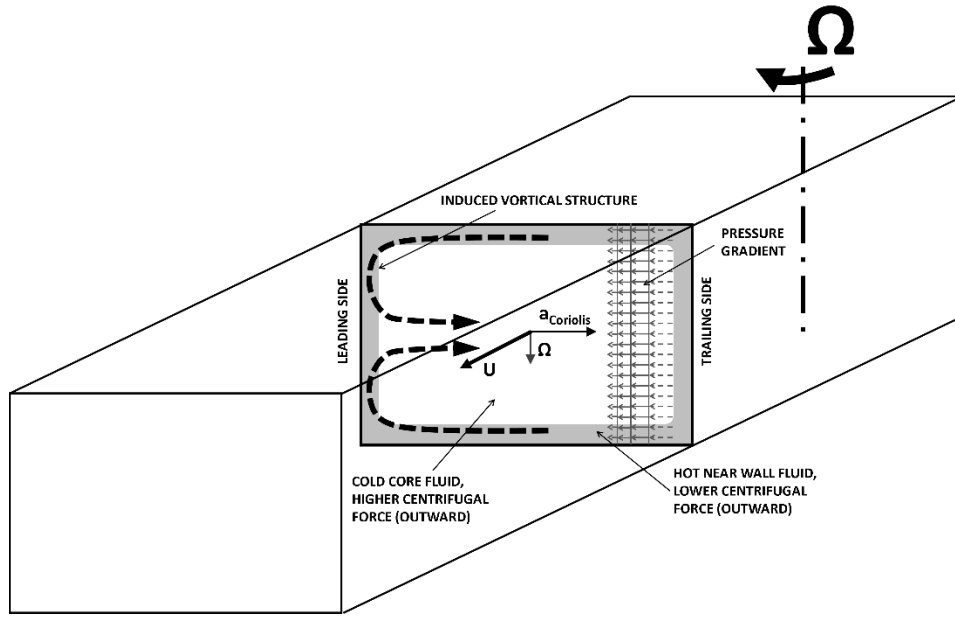


Figure 2

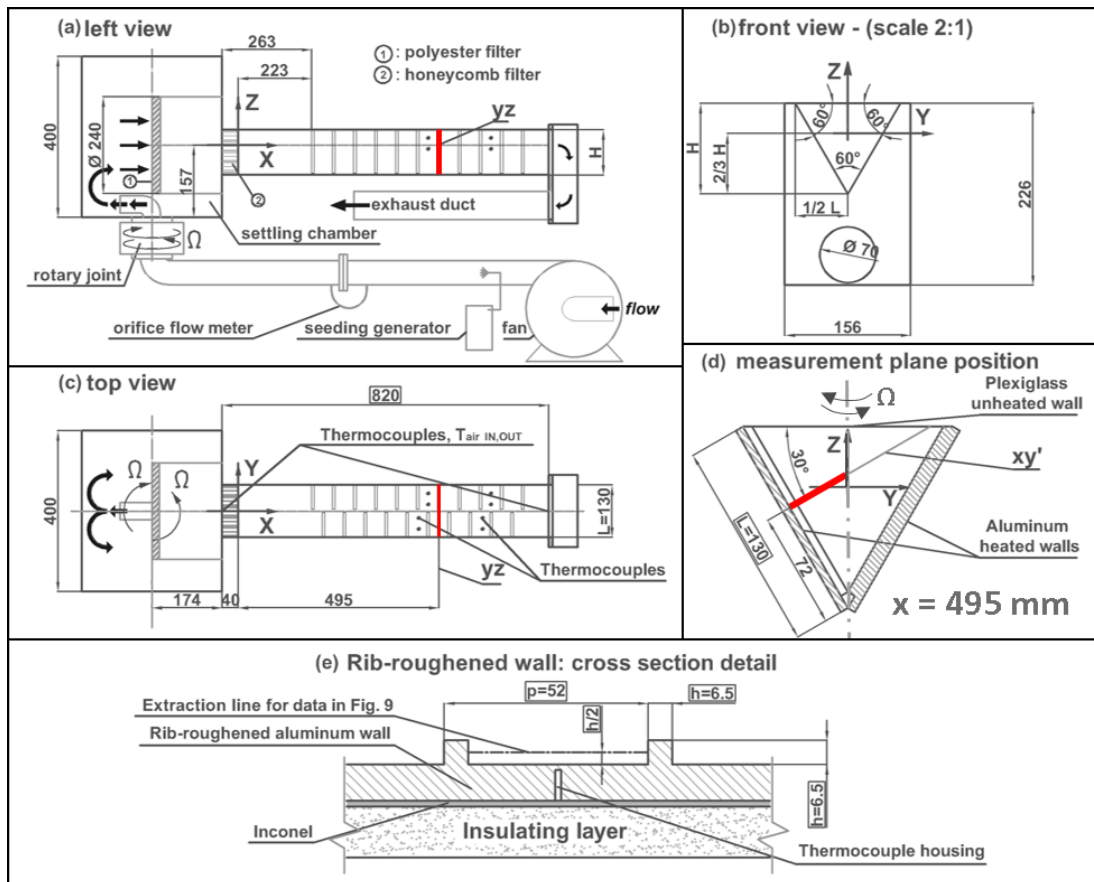
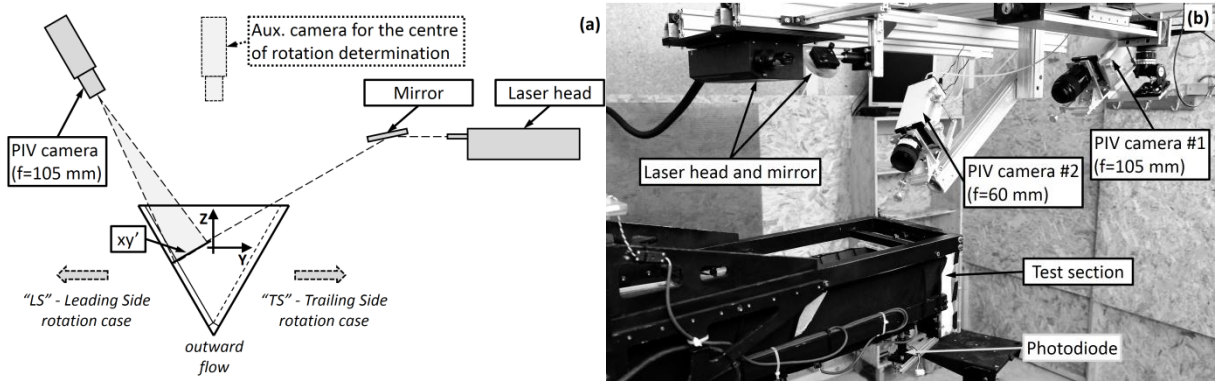


Figure 3



458

Figure 4

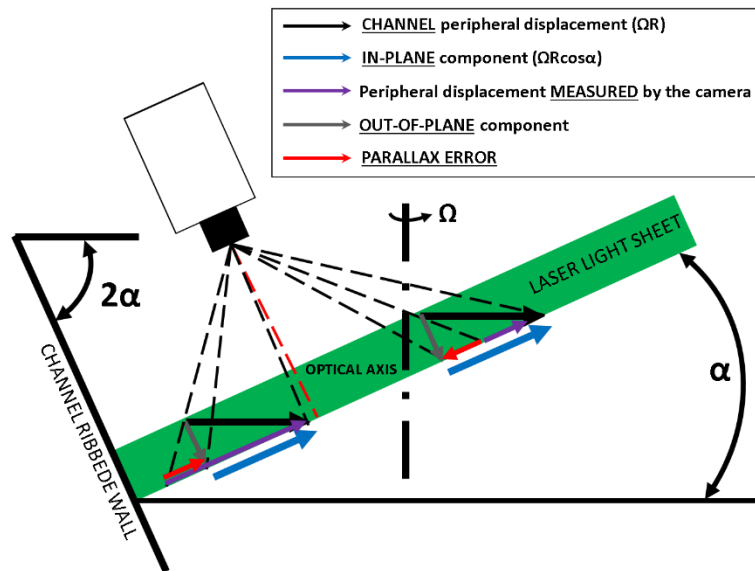


Figure 5

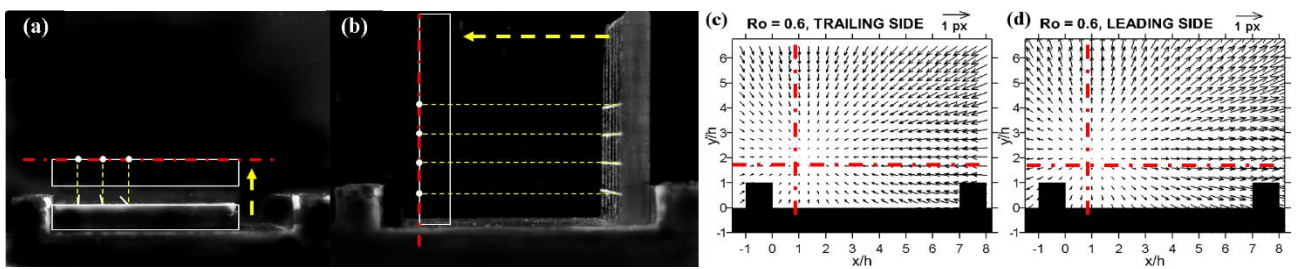


Figure 6

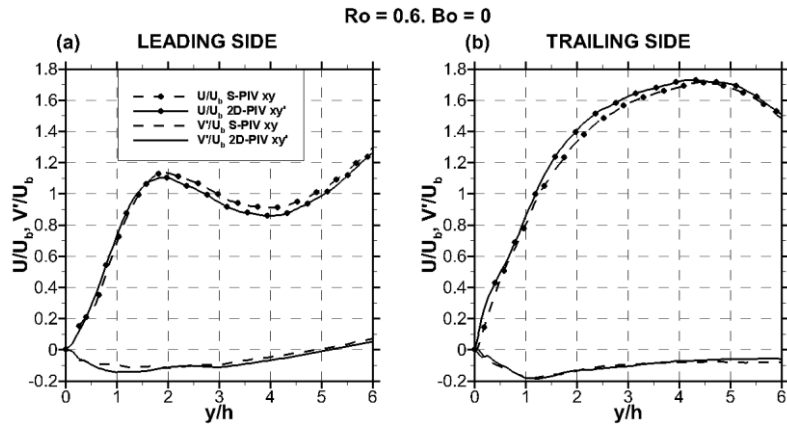


Figure 7

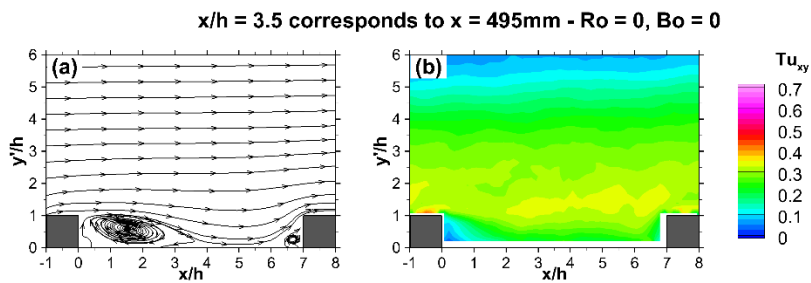


Figure 8

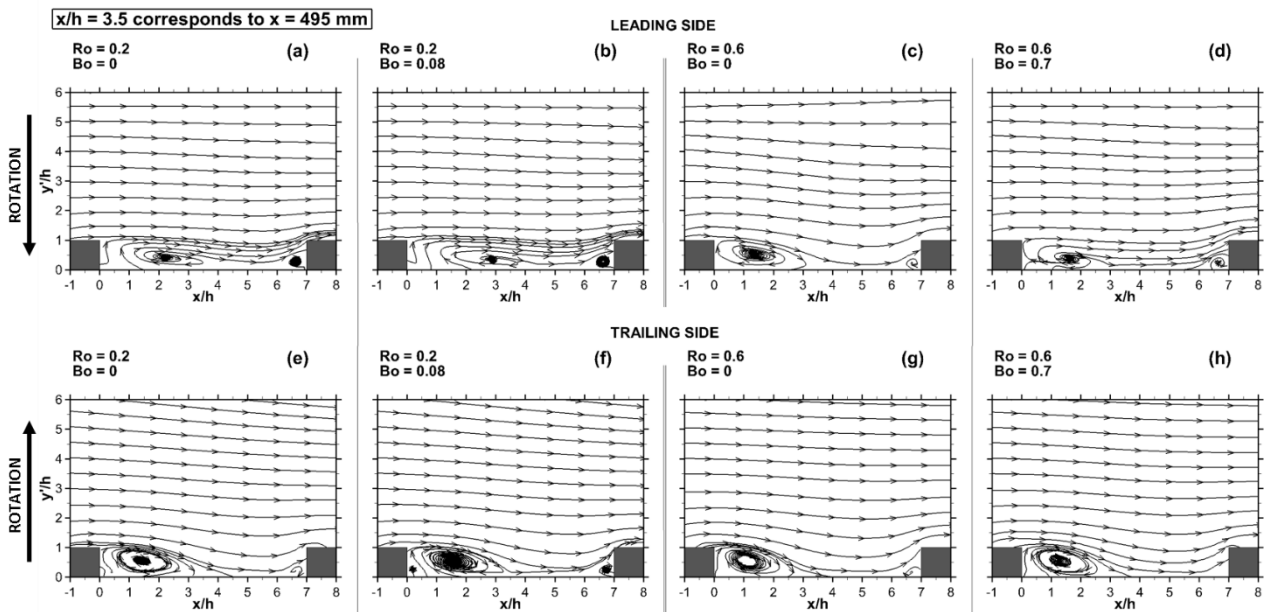


Figure 9

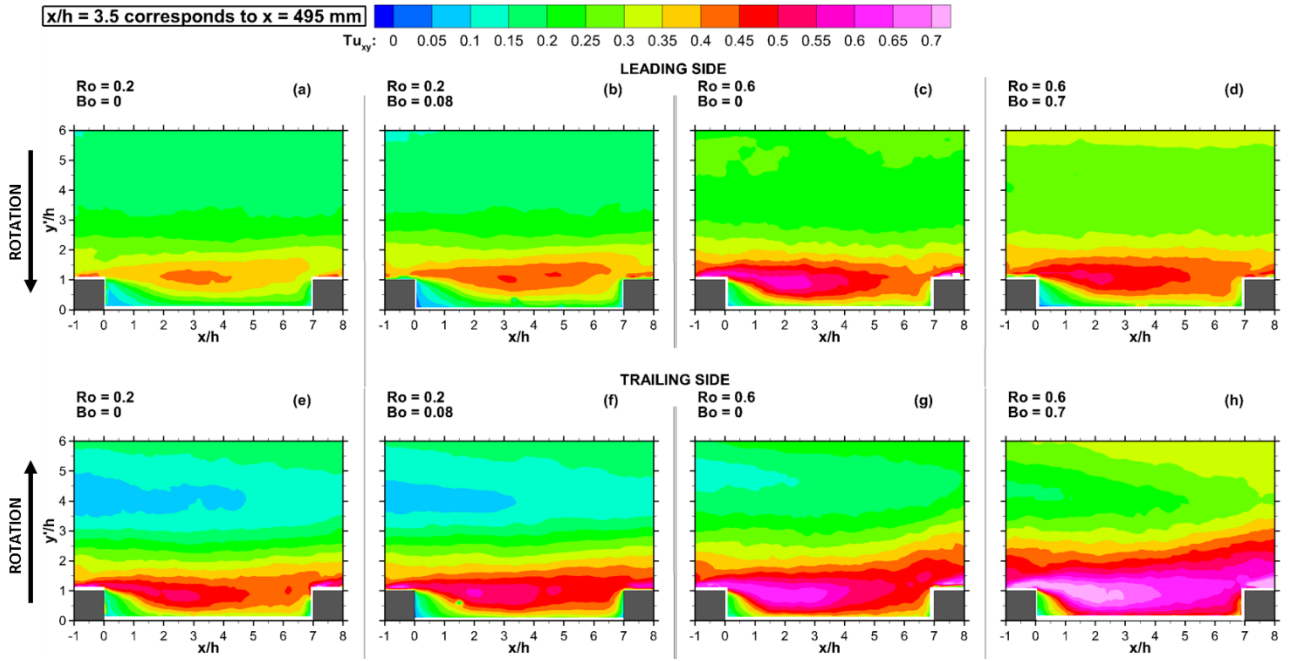


Figure 10

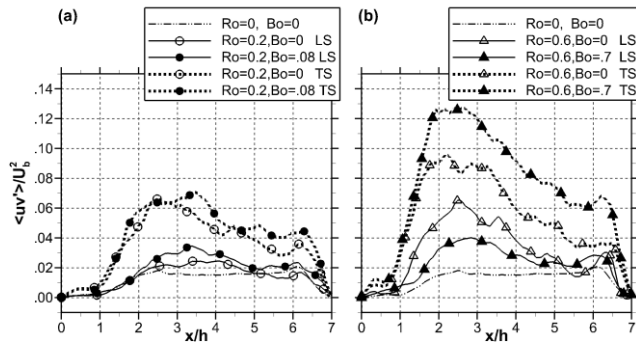


Figure 11

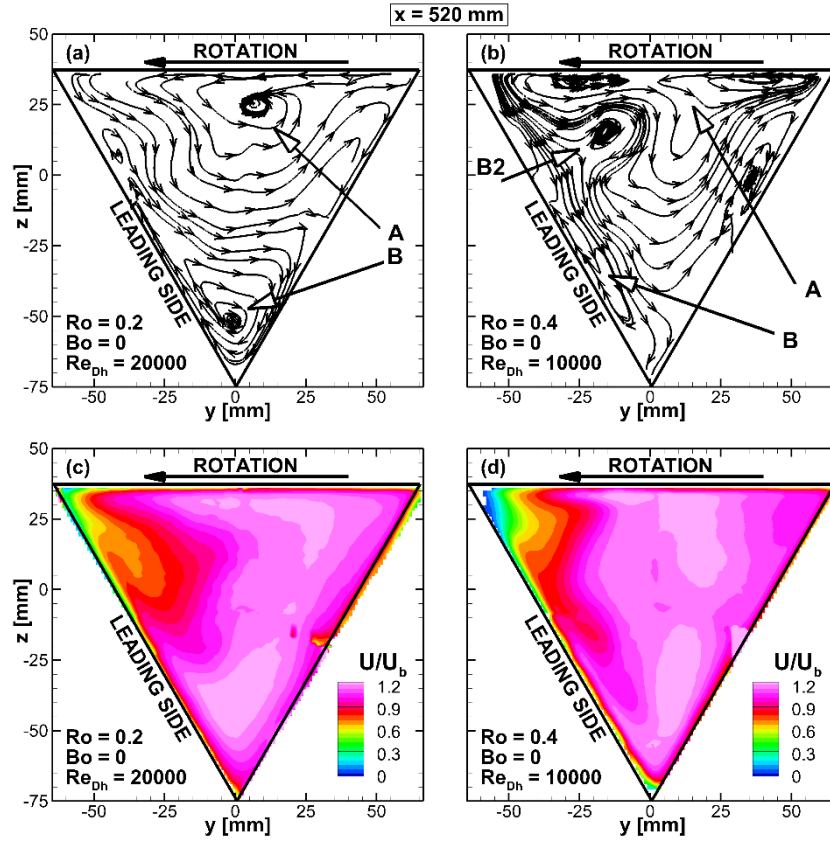


Figure 12

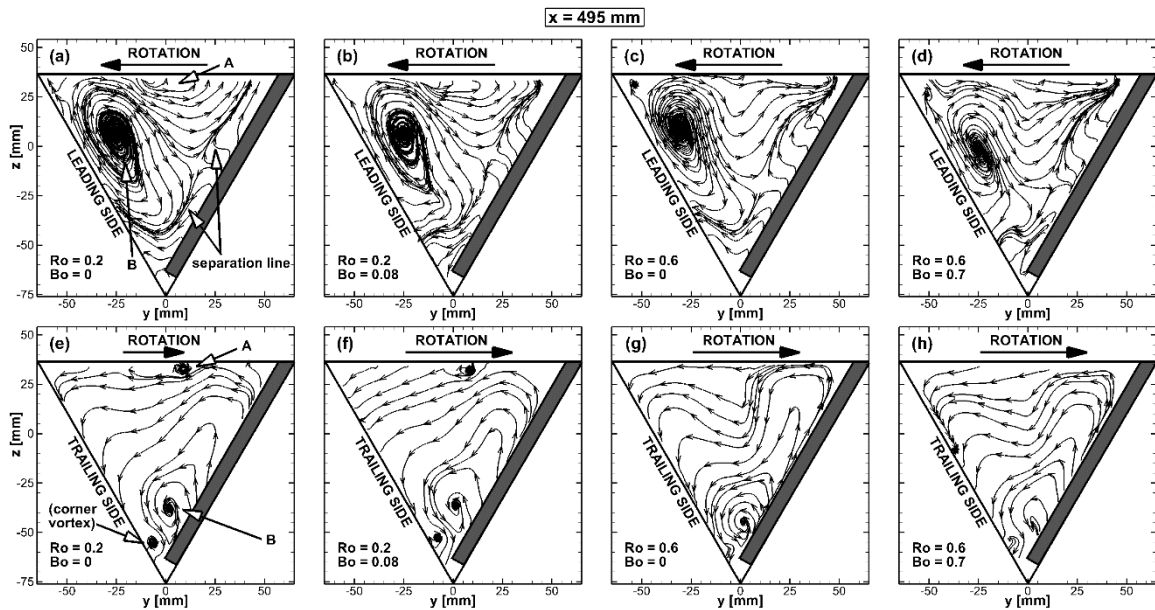


Figure 13

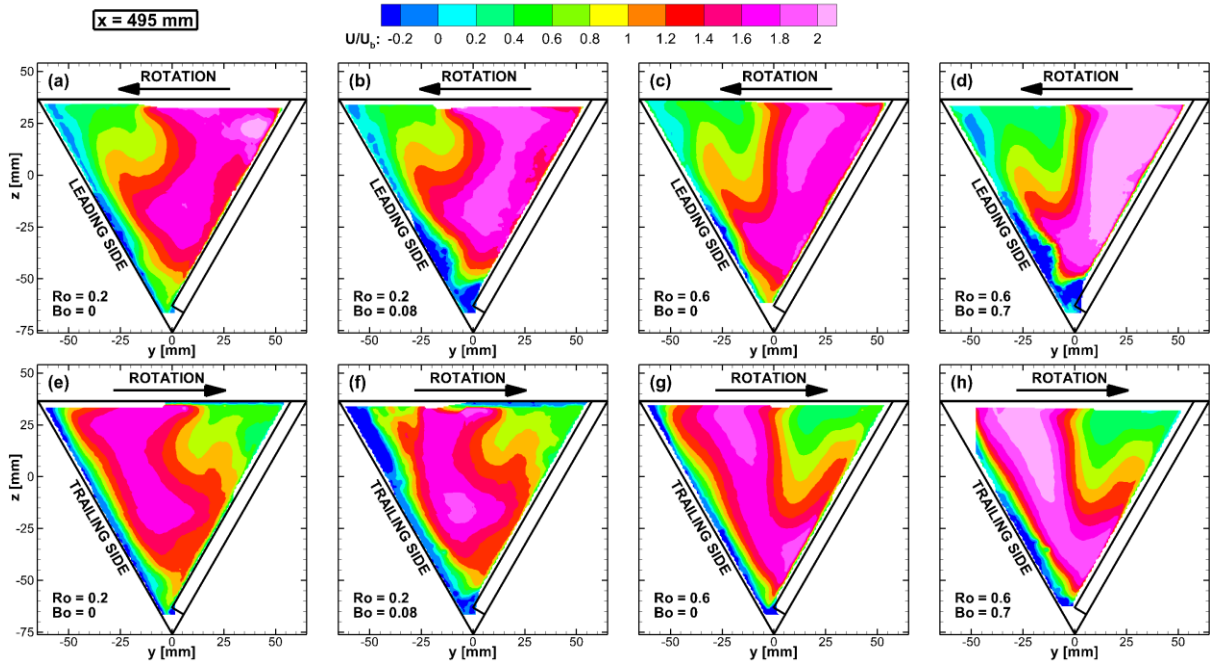


Figure 14

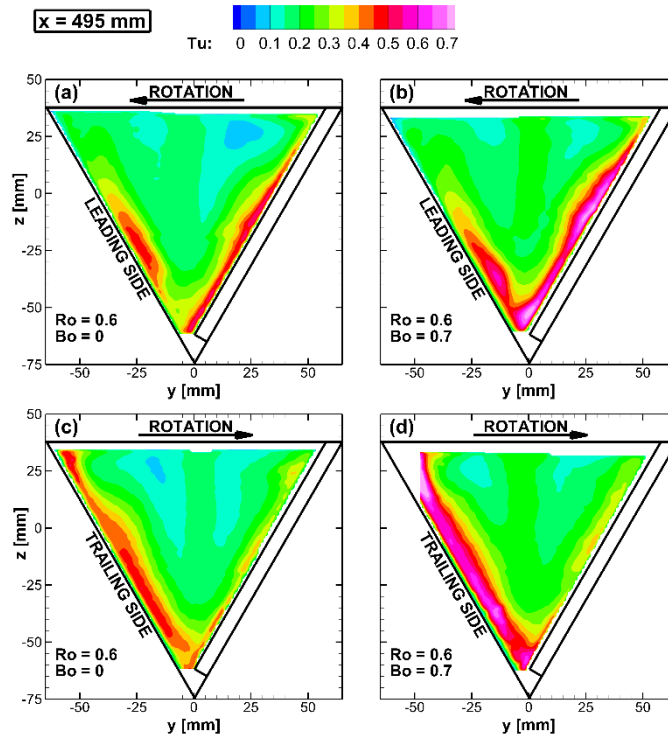
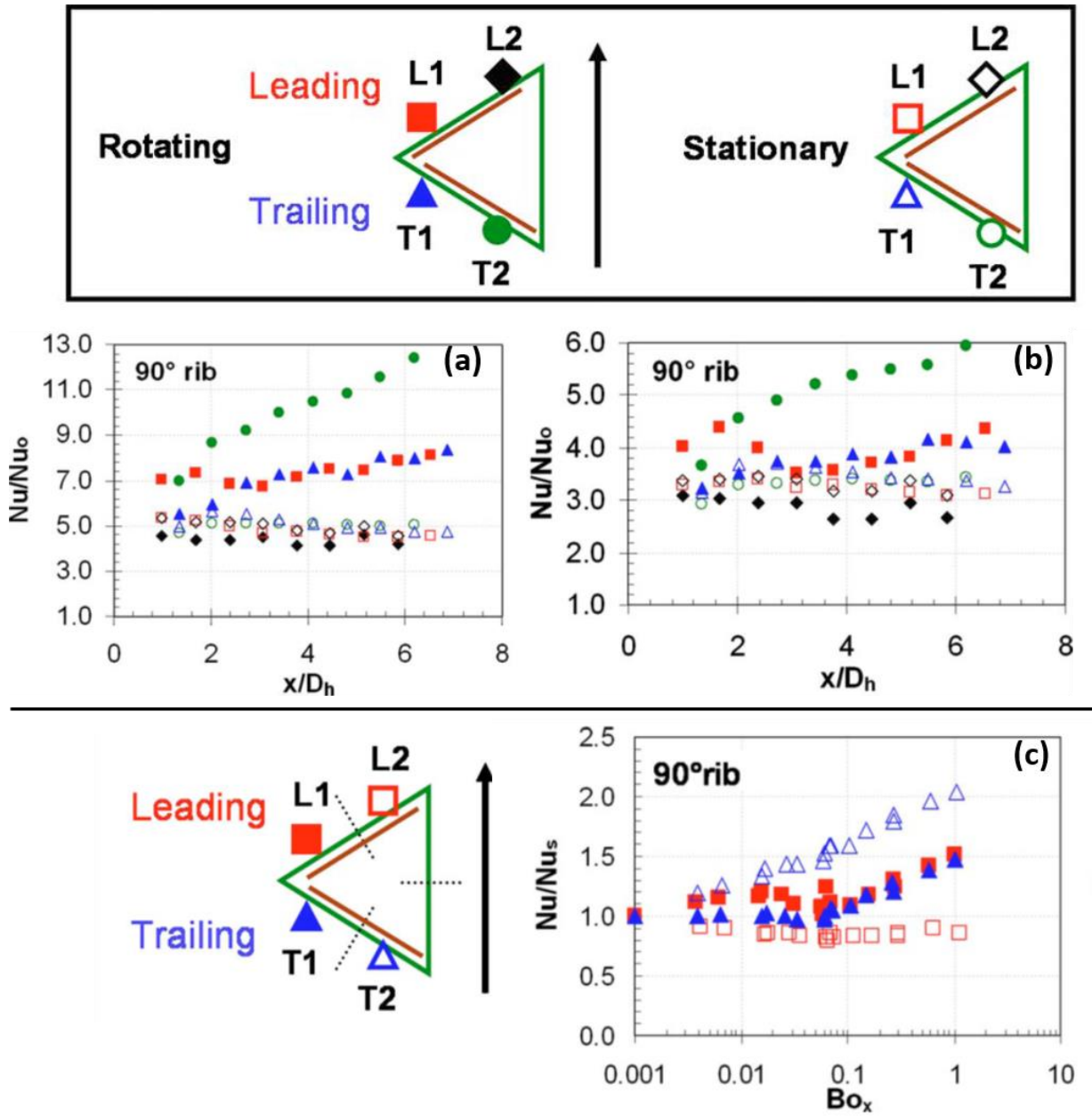


Figure 15



## List of Figures Captions.

Figure 1: Illustration of forces and main flows features found in a rotating duct

Figure 2: Experimental facility, nomenclature and positions of the PIV measurement planes (highlighted in red)

Figure 3: Measurement set-up used for 2D-PIV on plane  $xy'$  (a) and Stereo-PIV on plane  $yz$

Figure 4: Optical setup sketch and parallax error description

Figure 5: Parallax error compensation for 2D  $xy'$  measurements: examples of calibration by means of dedicated target displacement (a, b) and resulting optical axis position (red dashed lines) and displacement correction fields (c, d)

Figure 6: Comparison of 2D and Stereo-PIV data extracted on the intersection line of  $xy'$  and  $yz$  planes of  $U$  and  $V'$  profiles from 2D-PIV on  $xy'$  and S-PIV on  $yz$

Figure 7: Stream tracers and contour plot of the in-plane turbulence intensity in plane  $xy'$  for  $Ro=0$ .

Figure 8: Stream tracers in plane  $xy'$  for all the rotating cases.

Figure 9: Contour plots of the turbulence intensity in plane  $xy'$  for all the rotating cases.

Figure 10:  $\langle uv' \rangle$  Reynolds stresses component extracted at  $y'/h=0.5$  from plane  $xy'$ , (a) static vs  $Ro = 0.2$  and (b) static vs  $Ro = 0.6$  test cases.

Figure 11: Stream tracers (a, b) and contour plots of non-dimensional streamwise velocity component  $U/U_b$  (c, d) in plane  $yz$  for the smooth channel configuration (Pascotto et al., 2014).

Figure 12: Stream tracers in plane  $yz$  for all the rotating cases.

Figure 13: Contour plots of the non-dimensional streamwise velocity component  $U/U_b$  in plane  $yz$  for all rotating cases.

Figure 14:  $Tu$  levels in plane  $yz$  for  $Ro=0.6$

Figure 15: Nusselt number ratio distribution in the rotating channel (a –  $Re = 10000$ , 400 rpm, b -  $Re = 30000$ , 400 rpm) and effect of buoyancy parameter on Nusselt number ratios at  $x/Dh = 4.11$  (c) [12]